Triton
Numerical Survivability Report

DE-FOA-0001310: Next Generation Marine Energy Systems - Durability & Survivability
Award Number: DE-EE0007346
Principle Investigator: Tim Mundon. Ph.D.
Submission Date: September 28, 2018

Document contributes towards M3, D5

Following drawings provided:
<D8_Design_Drawings_Baseline+NonselectedApproaches.pdf>
<D8_Design_Drawings_Final_Design.pdf>

1. Table of Contents:

2. Summary / Scope

This report discusses the numerical modeling work performed for the Triton WEC. Detailed numerical modeling was carried out to assess system performance, in and out of survival mode, and to clearly understand how system loads vary across a range of conditions up to the 50-year extreme wave contour. A suite of numerical modeling tools, from mid-fidelity time domain models to high-fidelity CFD were used and compared. As a first step, we used laboratory experiments and CFD to study the reaction ring hydrodynamics over a range of oscillation conditions. This allowed us to refine our models of the full WEC system in order to improve model accuracy. We then used the mid-fidelity model and CFD to produce numerical predictions of system design loads, specifically the hydrostatic pressure loading, maximum tendon loads, and maximum mooring loads.

References

[1] T R Mundon, B J Rosenberg, and J van Rij, "Reaction Body Hydrodynamics for a Multi-DOF Point-Absorbing WEC". *Proc. 2017 EWTEC, Cork, Ireland.*

[2] R G Coe, B J Rosenberg, E W Quon, C Chartrand, Y Yu, J van Rij, and T R Mundon, "CFD design load analysis of a two-body wave energy converter" *Journal of Ocean Engineering and Marine Energy,* 2018 (under review).

3. Reaction Ring Hydrodynamics

Laboratory experiments and CFD

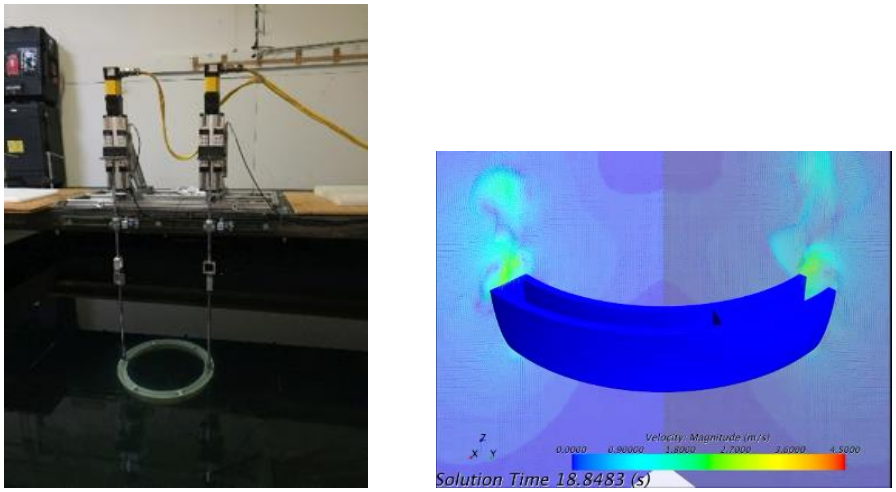

Figure 1. *(Left) Forced oscillation test bench to characterize reaction ring hydrodynamics. (Right) CFD simulation of reaction ring.*

OPI performed forced oscillation experiments to measure hydrodynamic coefficients for the Triton reaction ring across a range of scales. The aim was to identify scaling relationships and estimate the full-scale coefficients, thus enabling more accurate models of the full-WEC. Understanding scale dependence is identified as important, as although representative oscillation amplitudes can be generated in the laboratory (i.e. representative Keulegan-Carpenter numbers, *KC*), the dissimilitude between the laboratory and full-scale Reynolds numbers (*Re*) requires careful consideration when inferring full-scale coefficients from the experiments. To address and examine this, CFD was used to replicate a number of these model-scale tests and provide simulations at full-scale. CFD simulations were performed by NREL using STAR-CCM+ software.

The laboratory test facility consisted of a quiescent water basin (3.6 m in diameter, 1.15 m in depth) in which a geometrically scaled reaction ring was sinusoidally oscillated using a pair of linear actuators. The implementation of two actuators allowed the exploration of multi-modal response. Oscillating the two actuators in phase enabled characterization of the translational drag and added mass (heave), while oscillating the actuators out of phase enabled characterization of the rotational drag and added moments of inertia (equivalent to pitch and roll). For measurements in surge, which is equivalent to sway, the reaction ring was oscillated on its side using a single actuator. Measurements were completed for 1:75, 1:60, 1:50 and 1:36 scale reaction rings.

Figure 2. *Baseline Triton heave plate printed at 1:75, 1:60, 1:50 and 1:36 scale*

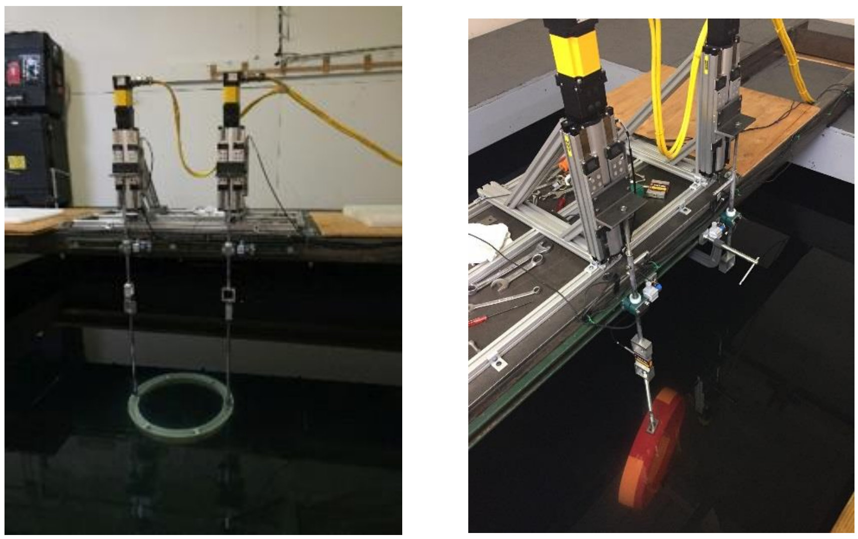

Figure 3. *(Left) Experimental arrangement for heave and pitch/roll. (Right) Experimental arrangement for surge/sway.*

Hydrodynamic coefficients

A time series motion and hydrodynamic force comparison between the tank experiments and CFD in heave is shown in Figure 4 and Figure 5. These tests were conducted at matching scale, oscillation amplitude, and frequency. The force time histories generally match well with amplitude agreement to within 20%.

Trends indicating how the hydrodynamic coefficients vary with *KC* and *Re* at all four experimental scales are shown in Figure 6, Figure 7, and Figure 8 for heave, pitch, and surge respectively. These properties (drag coefficient, C_d, and added mass coefficient, C_a) were derived by fitting the data to a Morison formulation. Also indicated are the coefficients obtained from CFD for a full-scale reaction ring.

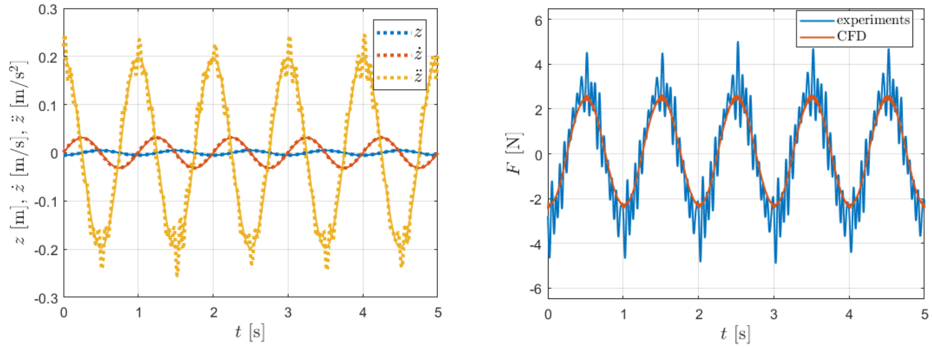

Figure 4. *Motion profiles (solid = CFD, dashed = experiments) and force profiles in heave at low KC number.*

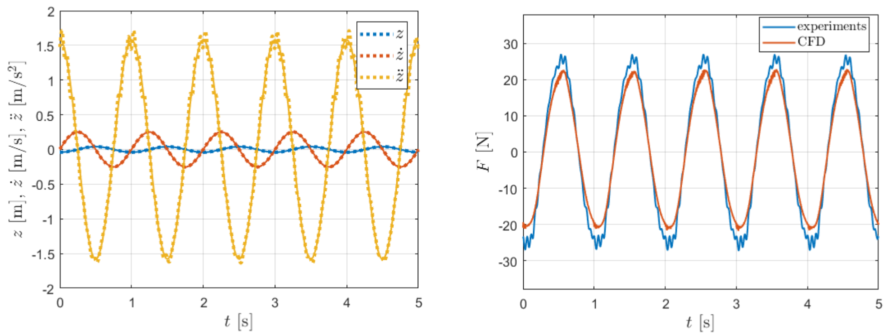

Figure 5. *Motion profiles (solid = CFD, dashed = experiments) and force profiles in heave at high KC number .*

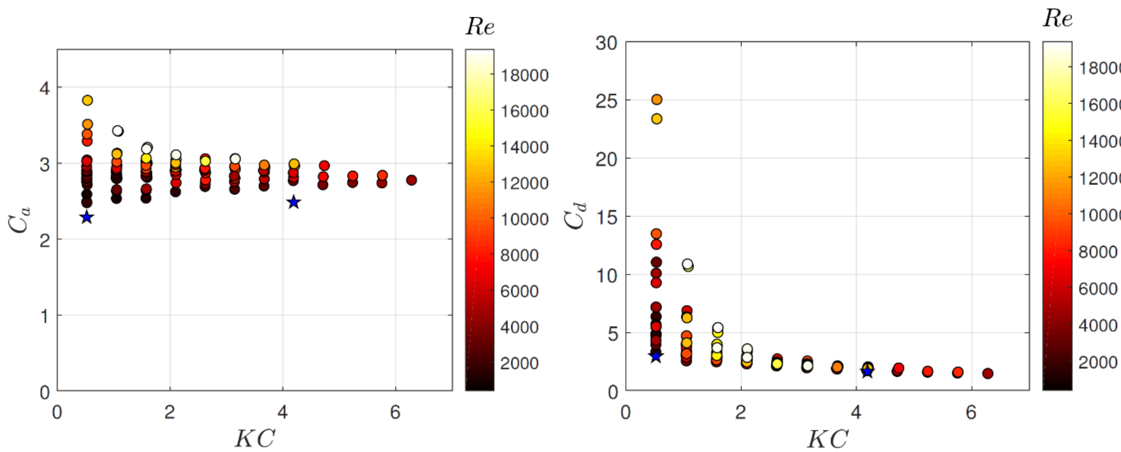

Figure 6. *Drag and added mass coefficients in* <u>*heave*</u> *for the 1:75, 1:60, 1:50, 1:36 reaction rings. The pentagram represents the coefficients obtained from CFD for a full-scale reaction ring.*

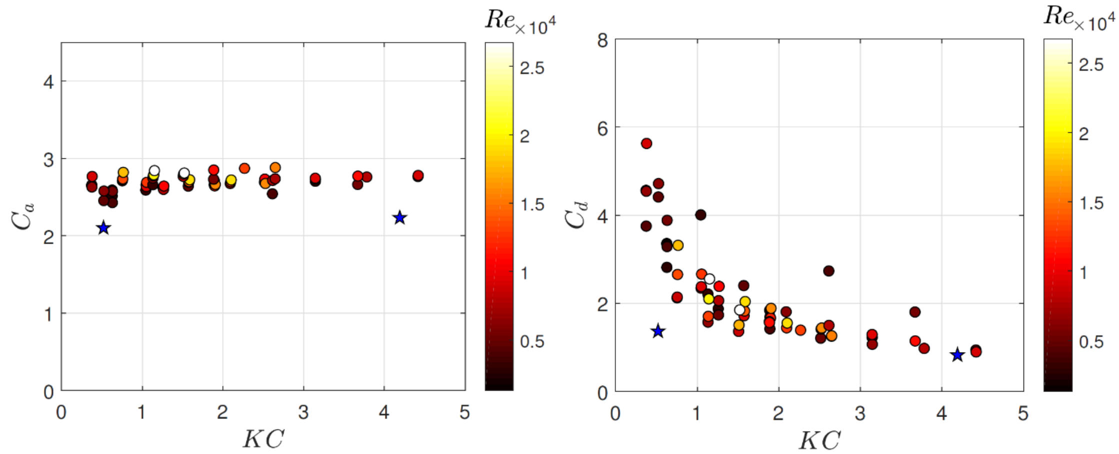

Figure 7. *Rotational drag and added MoI coefficients in* *pitch* *for the 1:75, 1:60, 1:50, 1:36 reaction rings. The pentagram represents the coefficients obtained from CFD for a full-scale reaction ring.*

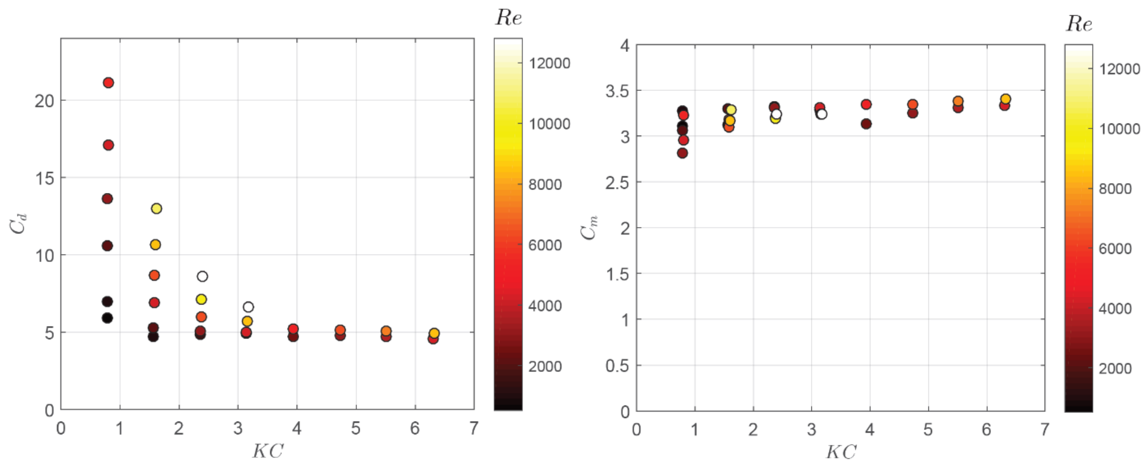

Figure 8. *Surge/sway coefficients measured at 1:75 scale.*

In general, the hydrodynamic coefficients obtained from experiments tend to asymptote to a fixed value for a given *KC* as *Re* increases. These scaling trends appear to confirm *Re* invariance above a certain threshold. With respect to added mass, C_a, there is overall a fairly good agreement between experiments and CFD, to within 20%. With respect to drag, at higher *KC* values the drag coefficients, C_d, agree well between experiments and CFD. However, a significant discrepancy was noted at low *KC* and high *Re*, where the experimental predictions at high *Re* are an order of magnitude above those from CFD. It should be appreciated that this discrepancy will not have a dramatic effect on the full-system model since the hydrodynamics are dominated by inertial (added mass) effects, however this deviation is interesting and will be the subject of future research.

It should be emphasized that for the aim of this project, which is to look at performance in extreme waves, the reaction ring will be in the high *KC* regime, where there is consistent agreement between experiments and CFD. Therefore, high confidence may be placed in these coefficients.

4. Mid-Fidelity Modeling

OrcaFlex model

A mid-fidelity numerical model of the Triton system was developed by OPI using the commercial hydrodynamic code Orcina OrcaFlex. The code solves for the multibody dynamics of the coupled marine and PTO systems, using the hydrodynamic coefficients derived from a frequency domain boundary element method (BEM) solver. For the surface float, the frequency-dependent added mass, damping, and linearized excitation forces were computed using the BEM solver Nemoh. The line dynamics for the tendons and moorings were solved in OrcaFlex using lumped mass finite-elements, and the PTO's were modelled by three spring-damper elements connected between the surface float and the top of each tendon.

Due to the large submergence depth of the reaction ring, it reacts minimally with the free surface and hence the wave radiation damping and wave excitation forces are negligible, as confirmed by Nemoh. As a result, the only hydrodynamic forces acting on the reaction ring are the added mass and viscous drag in each mode of motion and thus it can be modelled using a simple Morison formulation. As discussed in the precious section, OPI measured these hydrodynamic coefficients in multiple modes of motion using forced oscillation experiments, which were then validated by the National Labs using CFD. These coefficients were used to inform the OrcaFlex model.

OrcaFlex/WEC-Sim Comparison

In this project, NREL developed an additional mid-fidelity numerical model of the Triton system using the WEC-Sim solver. We then compared performance predictions between the WEC-Sim model, OPI's OrcaFlex model, and the 1:20 scale tank tests performed as part of the Wave Energy Prize. The aim was to determine the most accurate model to take forward in the project. Comparative results are shown in in Figure 10 for the irregular waves listed in Table 1.

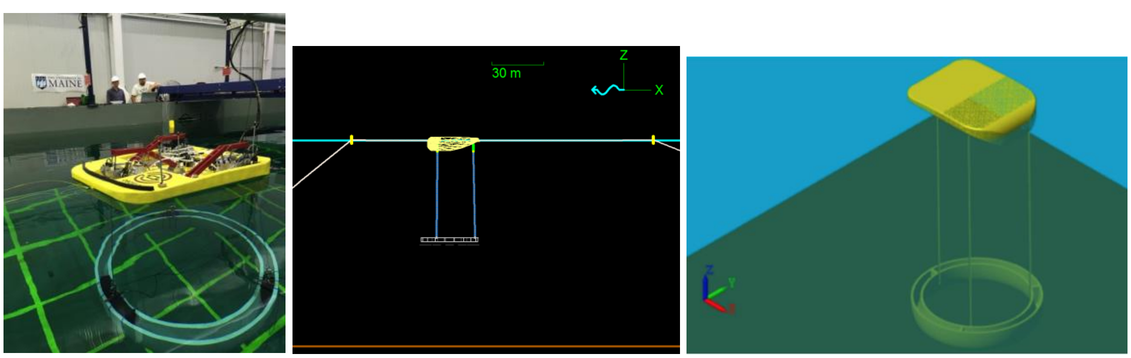

Figure 9. *1:20 physical model at UMaine W2 Basin (left). OrcaFlex model (center). WEC-Sim model (right).*

Table 1. *Full-scale irregular (Bretschneider) wave conditions tested for the 1:20-scale model at Carderock basin.*

Wave	**Tp (s)**	**Hs (m)**	**Direction**
IWS1	7.29	2.34	10°
IWS2	9.84	2.64	0°
IWS3	11.54	5.36	-70°
IWS4	12.70	2.06	-10°
IWS5	15.25	5.84	0°
IWS6	16.50	3.26	0°

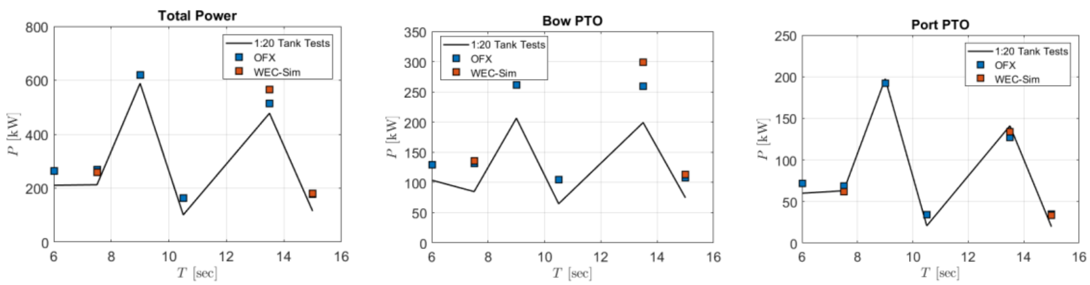

(a) Mean absorbed power.

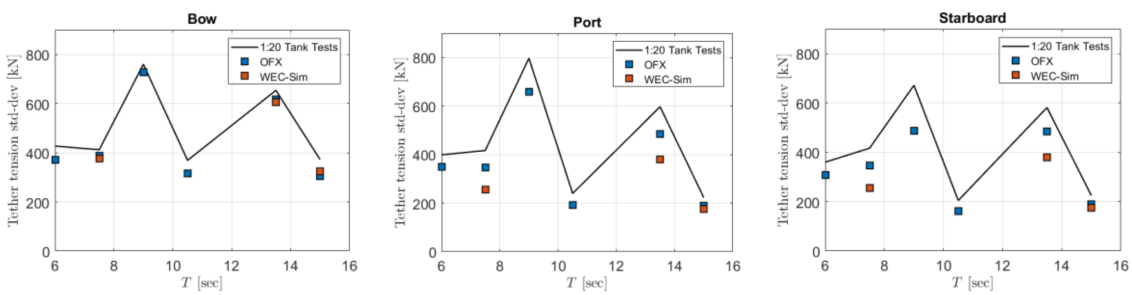

(b) Variation in tether tension (standard deviation)

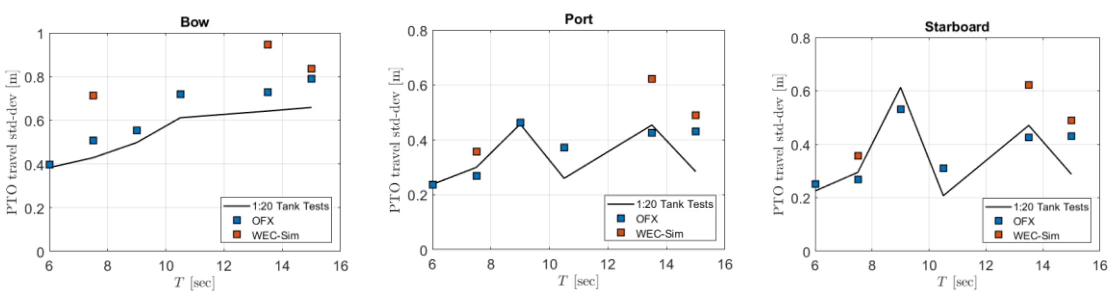

(d) Variation in PTO travel (standard deviation)

Figure 10. *Comparison of the OrcaFlex and WEC-Sim numerical models to basin tests at 1:20 scale in irregular waves.*

Presented in Figure 10 are the mean power, standard deviation of tendon tension, and standard deviation of PTO travel for each of the six wave conditions. With respect to these time-averaged statistics, both numerical models compare reasonably well against each other and to the wave basin tests, with the OrcaFlex model generally performing slightly better. This might be related to the more accurate line dynamics solver used in OrcaFlex for the tendons and moorings. A further comparison of a specific time-series is shown in Figure 11, demonstrating that the time-resolved dynamics are also captured quite well by OrcaFlex.

It was mutually agreed by OPI and the National Labs to proceed with the OrcaFlex mid-fidelity model to evaluate system loads in large waves and to generate Design Load Cases (DLC's). As OPI is more familiar with the OrcaFlex model and is better suited to perform this task, it was decided to focus the National Lab's time on developing and running the subsequent CFD analysis for the full-system.

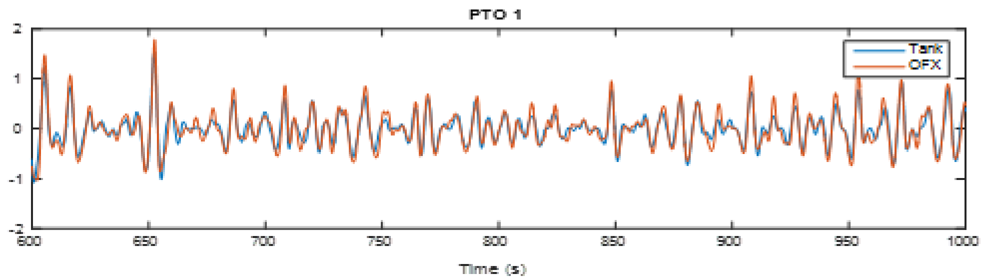

Figure 11. *Time-series comparison of the OrcaFlex numerical model and 1:20 scale tank tests (converted to full-scale) in the IWS2 wave condition. The curve represents the driving velocity of bow PTO.*

Survival mooring design

Using the OrcaFlex model, OPI developed a realistic 3-point mooring design capable of supporting the submerged Triton in survival mode, and did some work to optimize the mooring design.

As discussed in the Down-selection Report, the primary driver of the hull structural cost is the maximum submergence depth, and associated hydrostatic pressure loads, experienced in survival mode. Therefore, OPI numerically investigated different mooring designs that will minimize the hull submergence in the largest 50-year wave. Simulations suggest using shorter upper line segments to reduce the maximum submergence by providing a larger effective vertical restoring force on the WEC, as shown in Figure 13 and Figure 14.

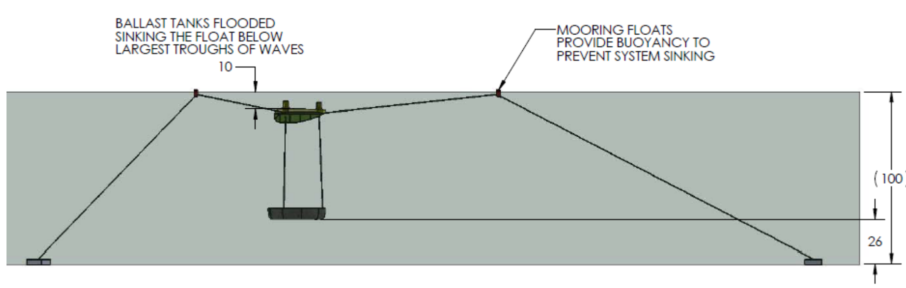

Figure 12. *Schematic of the submerged survival configuration.*

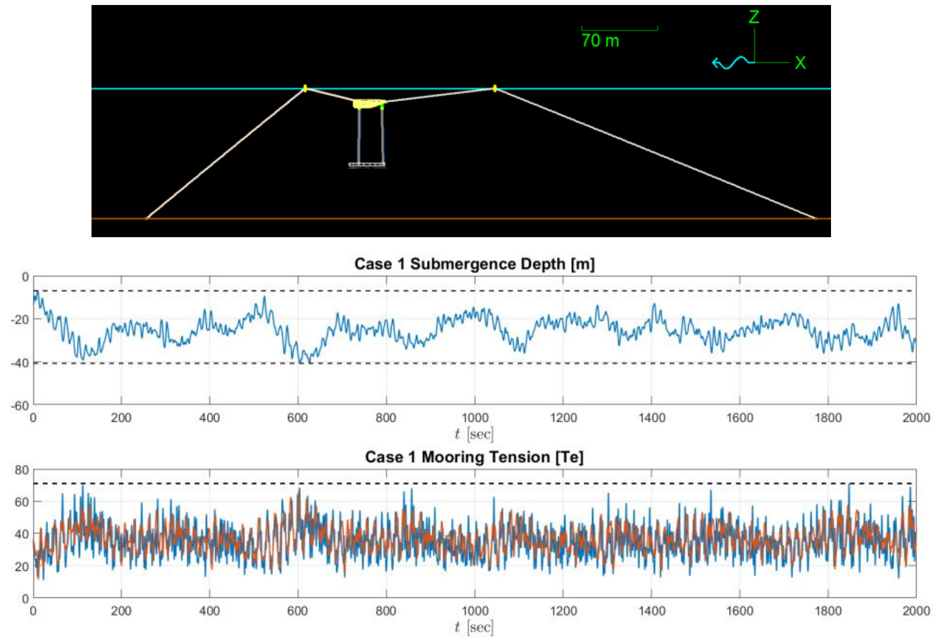

Figure 13. *OrcaFlex model of the baseline submerged survival configuration (100m upper lines).*

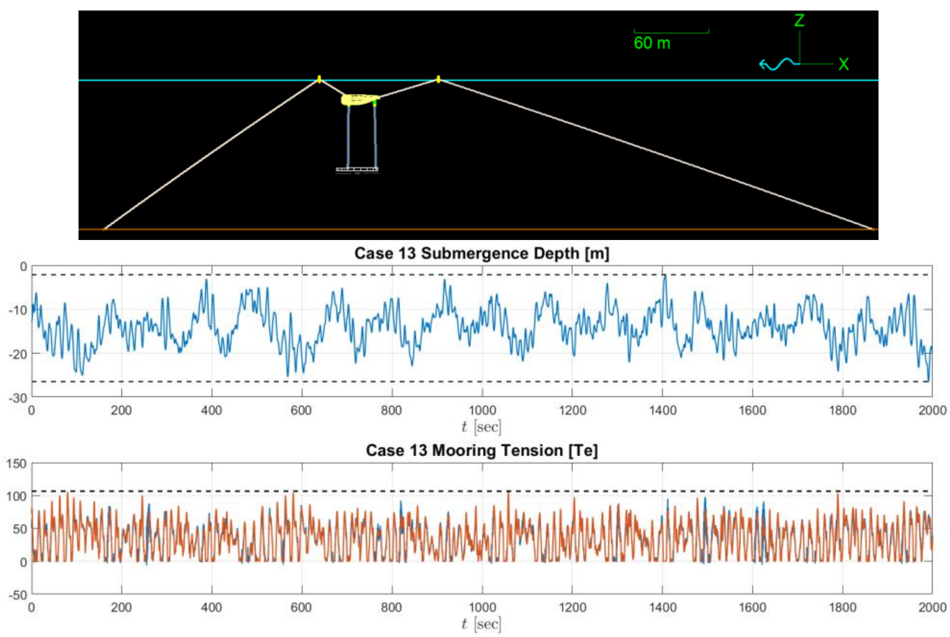

Figure 14. *OrcaFlex model of the improved submerged survival configuration (50m upper lines).*

Design loads

OPI analyzed Triton over a wide range of wave conditions, in floating (operational) and submerged (survival) configurations, using the mid-fidelity OrcaFlex model. Each wave condition was simulated using a Bretschneider spectrum for 2 hours with *dt* = 0.005. The results, summarized in Figure 15-Figure 17, show representative structural loading within the 50-year contour at Humboldt Bay, CA. Through discussion with Glosten, it was determined that the maximum tendon tension, maximum mooring tension, and maximum submergence depths are appropriate proxies for the global loads, which can be used to design the surface float structure.

Maximum Tether Tension (kN)

Tp (s)	4.9	6.3	7.7	9.2	10.6	12.0	13.4	14.8	16.2	17.6	19.0	20.4
Te (s)	4.2	5.4	6.6	7.8	9.0	10.3	11.5	12.7	13.9	15.1	16.3	17.5
Tz (s)	3.5	4.5	5.5	6.5	7.5	8.5	9.5	10.5	11.5	12.5	13.5	14.5
Hs (m)												
0.25												
0.75			4721		4682							
1.25									4628			
1.75				5178		5020						
2.25												
2.75					5976		5748		5268		5066	
3.25												
3.75				7250		7084			6029		5473	
4.25				8057	7862	7476	6911	6803	6578	6326		
4.75				8529	8331	7745	7179	7110	7056	6559		
5.25									7037	6752	6563	6419
5.75							4555		4554		6909	6663
6.25					4593						7003	6884
6.75						4614			4596			
7.25							4618					
7.75											4692	
8.25								4638				
8.75									4719			
9.25										4799		
9.75											4836	4864

Operational (Hs 0.25–6.25); Submerged (Hs 6.75–9.75); 50-year Contour

Figure 15. *Maximum tendon tension as a function of wave condition.*

Maximum Mooring Tension (kN)

Tp (s)	4.9	6.3	7.7	9.2	10.6	12.0	13.4	14.8	16.2	17.6	19.0	20.4
Te (s)	4.2	5.4	6.6	7.8	9.0	10.3	11.5	12.7	13.9	15.1	16.3	17.5
Tz (s)	3.5	4.5	5.5	6.5	7.5	8.5	9.5	10.5	11.5	12.5	13.5	14.5
Hs (m)												
0.25												
0.75			114		157							
1.25									250			
1.75				192		309						
2.25												
2.75					345		397		448		367	
3.25												
3.75				640		582			597		511	
4.25				788	645	705	742	783	716	663		
4.75				947	741	797	840	896	807	749		
5.25									901	848	792	705
5.75							453		601		879	791
6.25					623						990	889
6.75						641			647			
7.25							768					
7.75											534	
8.25								826				
8.75									745			
9.25										647		
9.75											600	601

Operational (Hs 0.25–6.25); Submerged (Hs 6.75–9.75); 50-year Contour

Figure 16. *Maximum mooring tension as a function of wave condition.*

Maximum Submergence Depth (m)

Tp (s)	4.9	6.3	7.7	9.2	10.6	12.0	13.4	14.8	16.2	17.6	19.0	20.4
Te (s)	4.2	5.4	6.6	7.8	9.0	10.3	11.5	12.7	13.9	15.1	16.3	17.5
Tz (s)	3.5	4.5	5.5	6.5	7.5	8.5	9.5	10.5	11.5	12.5	13.5	14.5
Hs (m)												
0.25												
0.75												
1.25												
1.75												
2.25												
2.75												
3.25												
3.75												
4.25												
4.75												
5.25												
5.75							-20		-24			
6.25					-19							
6.75						-22			-25			
7.25							-24					
7.75											-26	
8.25								-26				
8.75									-27			
9.25										-28		
9.75											-28	-28

Operational (Hs 0.25–6.25); Submerged (Hs 6.75–9.75); 50-year Contour

Figure 17. *Maximum hull submergence depth as a function of wave condition.*

As shown in the above contour plots, we have provided a demarcation between when the WEC is in operational mode versus submerged survival mode. This operational threshold was defined such that slack-tendon and end-stop events are completely avoided. A discussion on the effects of lowering this threshold contour is described in the Final Technical Report.

The results from this model demonstrate that the maximum mooring and tendon (and hence drivetrain) loads occur when the WEC is in the 'operational' configuration while the maximum hydrostatic pressure loads occur when the WEC is in the submerged 'survival' configuration. Specifically, the largest tendon loads tend to occur near device resonance, whereas the largest mooring loads appear to occur for longer wave periods. It can be seen that the largest hydrostatic pressure loads are driven by the maximum submergence depth in survival mode.

5. CFD Analysis

Sea state definition

From these mid-fidelity model results, OPI and the National Labs down-selected four wave conditions to explore at higher fidelity using CFD. It was determined that it would be challenging to accurately predict the maximum submergence depth using CFD. Due to the computational intensity required, only ~100 seconds may be simulated within a reasonable timeframe. However, the OrcaFlex simulations suggest that large variations in submergence depth tend to result from slower, second-order mooring dynamics, which occur on a time scale of 100's of seconds. Furthermore, the CFD software does not have an accurate mooring line dynamics solver like OrcaFlex, and therefore a simpler linear 'spring' representation for the mooring must be used. This simplification is expected to be sufficient for modeling the horizontal forces in 'operational' configuration, however it is expected to be less accurate in modeling the vertical restoring force provided by the mooring in 'survival' configuration. For these two reasons, we anticipated that CFD simulations of Triton in the submerged survival mode are unlikely to provide any more insight than the OrcaFlex results. Ultimately, it is expected that the 1:30 physical model tests (Task 4) will be the most accurate and representative indicators of maximum submergence depth.

Therefore, OPI and the National Labs decided to evaluate wave conditions on the extreme *operational* contour with the aim to obtain high-fidelity predictions of maximum tendon and mooring loads. From the results of the mid-fidelity simulations, two design-load case sea states of interest were chosen (``SS01'' and ``SS02''), summarized in Table 2. Since it is computationally infeasible to simulate a long-duration irregular sea in CFD, two simpler design wave realizations were defined for each sea state of interest: an equivalent *regular* wave and a *focused* wave. Thus, from the two design-cases selected we define a total of four sea states for evaluation. The two regular wave cases are referred to as SS01-R and SS02-R, respectively. Likewise, the focused waves are referred to SS01-F and SS02-F.

Table 2. *Design load cases for CFD.*

ID	Sig. wave height, H_s [m]	Peak period, T_p [s]	Max tendon load [MN]	Max mooring load [MN]	Peak wave-length, λ_p [m]	Peak phase speed, c_p [m/s]	Eq. reg. wave height, H_{reg} [m]
SS01	4.75	9.2	8.53	0.947	132	14.4	9.0
SS02	5.25	16.2	7.04	0.901	410	25.3	9.9

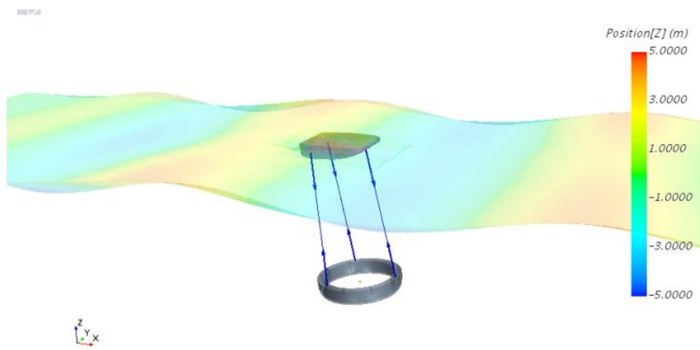

Figure 18. *CFD simulation of Triton WEC in a monochromatic wave (SS01-R).*

Regular (monochromatic) design waves are, in effect, a simplified representation of a highly peaked wind-generated fetch-limited sea. At the limit, the energy bandwidth of the sea approaches zero, and we are left with a regular wave. A *regular* wave of H = $1.9H_s$ was used to approximate the largest individual wave within the corresponding *irregular* sea. The factor of 1.9 comes from the common assumption of wave amplitudes following a Rayleigh distribution. A CFD animation of case SS01-R is shown in Figure 18. The focused wave approach involves exciting the WEC with a broadband impulse. In this case, the OrcaFlex simulation results were used to produce wave and response spectra for the quantities of interest (e.g. tendon tension), and from these responses, the most-likely extreme response (MLER) method was used to develop a corresponding focused wave.

Design loads

Table 3. *Maximum (bow) tendon load.*

Sea State	CFD – regular	CFD – focused	OrcaFlex	Tank Tests
SS01	8.27	7.49	8.53	8.40
SS02	4.73	5.81	7.04	7.22

Table 4. *Maximum mooring load.*

Sea State	CFD – regular	CFD – focused	OrcaFlex	Tank Tests
SS01	0.819	0.394	0.947	0.840
SS02	0.328	0.428	0.901	0.720

Table 3 and Table 4 summarize the maximum tendon and mooring loads achieved using four different approaches: an equivalent regular wave in CFD, an equivalent focused wave in CFD, a long-duration (2 hour) irregular wave simulation in Orcaflex, and a long-duration (1-1.5 hour) irregular wave test using a physical model (from Task 4).

Comparison between CFD, mid-fidelity model, and experiments

Overall, the CFD results provided mixed levels of accuracy. For example, cases SS01-R and SS02-F predicted the maximum tendon tension to within 2% and 11%, respectively, compared to the tank tests. However, cases SS02-R and SS02-F under predicted maximum tendon loads by 20-35% compared to the tank tests. Except for SS01-R, which was accurate to within 3%, the maximum mooring loads for the other CFD cases were under predicted by 40-55% compared to the tank tests. Part of this deviation might be explained by the simplified mooring model (i.e. a linear spring) implemented in CFD, and future work might involve might involve coupling the CFD software to an external mooring model.

The varying levels of accuracy between the CFD and tank tests could be attributed to two explanations: inaccuracies in the CFD calculation, or inability of the simplified design waves (i.e. regular and focused waves) to reliably predict the maximum loads in the corresponding irregular sea. To address this question, OPI replicated the four CFD cases in the physical model tank tests (Task 4).

Figure 19 compares the experimental and CFD data for regular wave case SS02-R. This demonstrates that the peak tendon tension for the regular wave CFD simulation and regular wave tank test agree to within 10%, however, both of these results are 30% below the value achieved in the long duration irregular tank test. The mooring load fluctuation is nearly equivalent between the experiments and the CFD in the regular wave condition. The apparent discrepancy arises because in the physical model, the system drifts downwave, thus increasing the mean tension and resulting in the vertical shift between the two curves. This downwave drift is not apparent in the CFD, possibly due to the short duration of the simulations (less than 10 cycles).

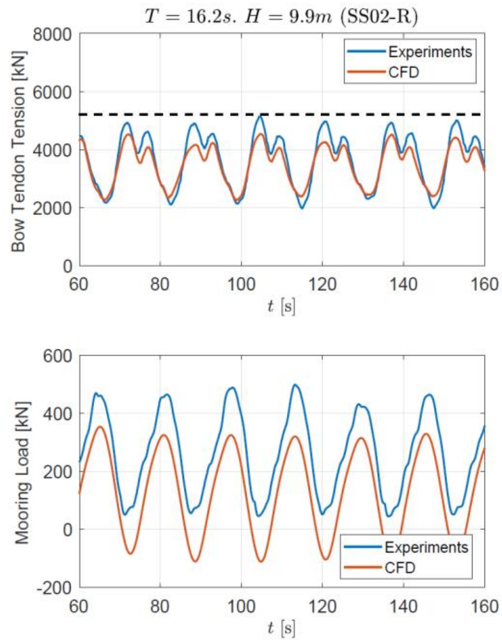

Figure 19. *Comparison between physical model tests and CFD for monochromatic wave SS02-R.*

Figure 20 compares the experimental and CFD data for focused wave case SS02-F. Again, while there is reasonable agreement in system response between the experiments and CFD, the focused wave approach tends to under predict the maximum system loads compared to the long duration irregular tank test.

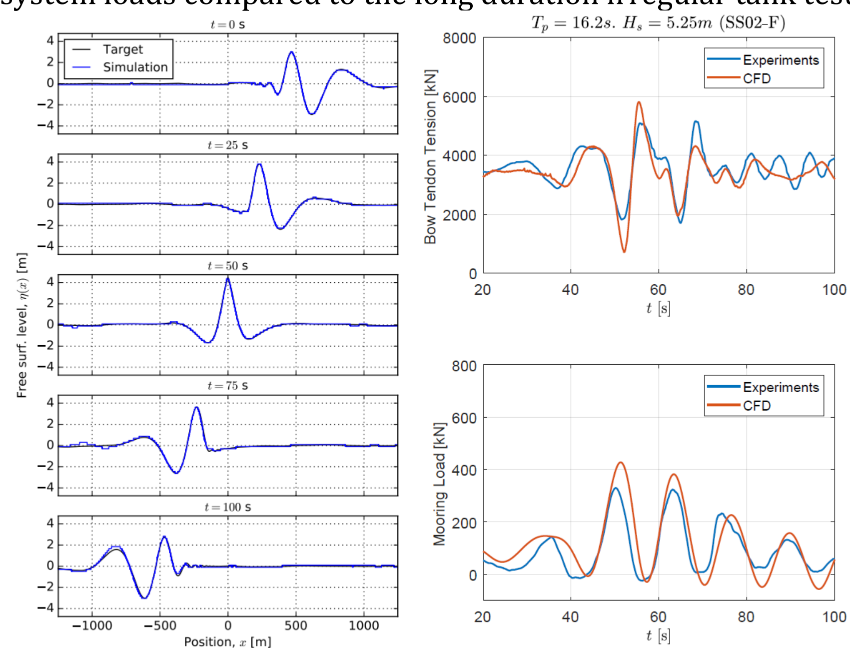

Figure 20. *(Left) Target and achieved focused wave in CFD. Device is at x=0. (Right) Comparison between physical model tests and CFD for focused wave SS02-F.*

From this analysis, it can be concluded that the CFD captures the system dynamics reasonably well and is a fairly accurate model. However, the design loads produced from the monochromatic and focused wave approximations had varying levels of reliability. Ultimately our results suggest that, if possible, it is best practice to obtain design loads from physical model testing.